Mechanism of shaping membrane nanostructures of endoplasmic reticulum

Ben Zucker[a] and Michael M. Kozlov[a,1]

[a]Department of Physiology and Pharmacology, Sackler Faculty of Medicine, Tel Aviv University, Tel Aviv–Yafo 6997801, Israel

Edited by James Hurley, Department of Molecular and Cell Biology, California Institute for Quantitative Biosciences, University of California, Berkeley, CA; received September 2, 2021; accepted November 17, 2021

Recent advances in super-resolution microscopy revealed the previously unknown nanoscopic level of organization of endoplasmic reticulum (ER), one of the most vital intracellular organelles. Membrane nanostructures of 10- to 100-nm intrinsic length scales, which include ER tubular matrices, ER sheet nanoholes, internal membranes of ER exit sites (ERES), and ER transport intermediates, were discovered and imaged in considerable detail, but the physical factors determining their unique geometrical features remained unknown. Here, we proposed and computationally substantiated a common concept for mechanisms of all ER nanostructures based on the membrane intrinsic curvature as a primary factor shaping the membrane and ultra-low membrane tensions as modulators of the membrane configurations. We computationally revealed a common structural motif underlying most of the nanostructures. We predicted the existence of a discrete series of equilibrium configurations of ER tubular matrices and recovered the one corresponding to the observations and favored by ultra-low tensions. We modeled the nanohole formation as resulting from a spontaneous collapse of elements of the ER tubular network adjacent to the ER sheet edge and calculated the nanohole dimensions. We proposed the ERES membrane to have a shape of a super flexible membrane bead chain, which acquires random walk configurations unless an ultra-low tension converts it into a straight conformation of a transport intermediate. The adequacy of the proposed concept is supported by a close qualitative and quantitative similarity between the predicted and observed configurations of all four ER nanostructures.

endoplasmic reticulum | membrane curvature | membrane shaping | membrane elasticity | membrane nanostructures

Endoplasmic reticulum (ER) is the largest and one of the central membrane-bound organelles of eukaryotic cells (1–3) whose crucial functions include the protein and lipid synthesis, exchanging the produced molecules with other intracellular organelles, and wrapping the nucleus (1). Related to its intracellular tasks, ER membrane is organized into highly intricate and inhomogeneous networks of interlinked nanotubules and sheets. ER networks exhibit a multiscale structure, which include macroscopic and nanoscopic levels of organization.

The nanoscopic ER structures were discovered only recently by super-resolution microscopy and are characterized by the internal length scales in the range of 10 to 100 nm (4, 5). The four types of the ER nanostructures are the ER tubular matrices (4), the nanoholes in ER sheets (5), the internal membrane arrangements of ER exit sites (ERES), and the ER transport intermediates (6).

The ER matrices are arrays of tightly packed intertubular three-way junctions connected by short tubules (4). The characteristic spacing between the junctions is of the order of 100 nm going, in some cases, down to about 50 nm (4). The ER matrices undergo rapid shape fluctuations, which include fast interconversions between the extremely dense and the relatively loose packing of the three-way junctions and strong undulations of the network plane. While, for the fluctuation reasons, the spatial arrangements of the junctions within the matrices look very irregular in most of the images, some snapshots reveal the junction packing in nearly regular nanoarrays (see Fig. 2*A*) (4).

The sheet nanoholes are circular dynamic pores of about 100 nm diameter formed in the ER sheet plane across the 30- to 50-nm-thick sheet lumen (5, 7, 8) (see Fig. 3*A*).

The ERES internal nanostructures appear as about 300-nm large grape-like ensembles of contiguous round membrane swellings of approximately 60 nm diameter (6) (see Fig. 4*E*). Upon transport initiation, ERES produces ER intermediate structures, which exhibit shapes of micrometer long, few tens of nanometers thick, pearled membrane tubes with periodic varicosities (6) (see Fig. 4*G*).

Due to the major effort of biological research over the last decade, the key proteins responsible for the generation of local curvatures of ER membranes have been largely identified (2, 9–11). Yet, the physical mechanisms determining the unique architecture of ER nanostructures have never been considered and represent the subject of this study.

Here, we proposed a common mechanism of shaping of all four ER nanostructures based on the homogeneous intrinsic curvature of the membrane as the major factor determining the membrane configurations. Our computations revealed a common structural motif underlying the architecture of most of ER nanostructures and having the origin in the geometry of surfaces of constant mean curvature. The ultra-low membrane tensions are suggested to serve as a shape-modulating factor. We obtained, computationally, the membrane shapes reproducing the experimentally observed geometrical features of the ER matrices, ER sheet nanoholes, ERES internal membranes, and ER transport intermediates. We predicted the existence of the energetically degenerated conformations of the ER matrices and described

Significance

A highly intricate architecture of endoplasmic reticulum (ER) membrane is crucial for the organelle functioning. Recent super-resolution microscopy studies discovered a nanoscopic level of ER organization characterized by 10- to 100-nm internal length scales. Deciphering the physical mechanisms of forming the ER nanostructures is a base for understanding the cell control of ER dynamics. Here, we proposed and computationally substantiated a common mechanism of shaping of all currently known ER nanostructures based on the intrinsic membrane curvature and ultra-low tensions as, respectively, a primary and a modulating factor.

Author contributions: M.M.K. designed research; B.Z. and M.M.K. performed research; B.Z. and M.M.K. analyzed data; and B.Z. and M.M.K. wrote the paper.

The authors declare no competing interest.

This article is a PNAS Direct Submission.

This open access article is distributed under Creative Commons Attribution-NonCommercial-NoDerivatives License 4.0 (CC BY-NC-ND).

[1]To whom correspondence may be addressed. Email: michk@tauex.tau.ac.il.

This article contains supporting information online at http://www.pnas.org/lookup/suppl/doi:10.1073/pnas.2116142119/-/DCSupplemental

Published December 20, 2021.

their architecture. We proposed the ultra-low tensions to support the most compact configuration of ER matrices, to promote formation the ER sheet nanoholes, and to drive the transformation of ERES membranes into the ER transport intermediates.

Model

We model the configurations of ER nanostructures as equilibrium membrane shapes corresponding to minima of the membrane elastic energy F_E. We define this energy as the thermodynamic work, which has to be performed for pulling the necessary amount of the membrane area A out of an effective membrane reservoir and shaping the pulled membrane into the conformation of the nanostructure.

The reservoir represents the ER membrane surrounding the nanostructure and is characterized by the elastic properties typical for the cylindrical ER tubules: the curvature in the elastically relaxed state referred below to as the intrinsic curvature J_0 (12), the bending modulus κ (13), and, generally, a tension γ. The intrinsic curvature J_0 accounts for the membrane-shaping effect of the curvature inducing proteins bound to the membrane surface, which in the case of ER are represented by the proteins of the reticulon and REEP families (14). We assumed the J_0 values to be in the range 0.1 to 0.01 nm^{-1}, corresponding to the assessments by different methods of the ER tubule radii (5, 15, 16). We assume $\kappa = 20 k_B T \approx 10^{-19} Joule$ (in which $k_B T$ is the product of the Boltzmann constant and the absolute temperature) typical for lipid bilayers (17). The reservoir tension γ will be taken as either vanishing or having ultra-low values up to 10 μN/m as can be deduced from the analysis of the ER tubule dynamics (18) and fluctuations (19).

The elastic energy F_E consists of the energy of membrane bending F_B and of membrane tension F_T

$$F_E = F_B + F_T. \quad [1]$$

The bending energy per unit membrane area is given by

$$f_B = \frac{1}{2}\,\kappa\,(J - J_0)^2, \quad [2]$$

where J is the total curvature (doubled mean curvature) of the membrane. Eq. **2** can be seen as Helfrich model (13) with accounting for a difference in the physical meaning between the intrinsic curvature J_0 and Helfrich's spontaneous curvature J_S (12).

The total bending energy F_B is obtained by integration of f_B over the surface of the nanostructure membrane

$$F_B = \oint f_B \mathrm{d}A. \quad [3]$$

The energy of the membrane tension F_T is given by

$$F_T = \gamma A. \quad [4]$$

The elastic energy minimization and computation of the nanostructure conformations are performed by the finite element method using Brakke's Surface Evolver program (20).

Results

ER Tubular Matrices. ER tubular matrices are polygonal networks of membrane tubules interconnected by three-way junctions (4). To understand the major features of the network architecture, we start with analyzing the equilibrium configurations of one polygonal unit cell connected directly to a reservoir and then extend the computations to an ensemble of several unit cells.

Single polygonal unit cell. Since the real ER tubular networks are irregular, we examine the unit cells of hexagonal, pentagonal, quadratic, and triangular symmetries. For an illustration of the notations, we use one of the computed configurations (Fig. 1*A*).

A unit cell is linked to the reservoir along border lines whose number is equal to that of the three-way junctions (Fig. 1*A*). The border lines are circles with radius $\frac{1}{J_0}$ corresponding to the cross-section of the reservoir's tubules (Fig. 1*A*). To guarantee the smoothness of transition between the unit cell membrane and that of the reservoir, the former must be perpendicular to the border line plane (Fig. 1*A*), which serves as a boundary condition. In order to minimize the possible effects of the boundary conditions on the calculated configurations, we took the distance R between the border lines and the unit cell center to substantially exceed the internal scale $\frac{1}{J_0}$ and equal $R = \frac{18}{J_0}$ or $\frac{24}{J_0}$.

First, we considered the case of vanishing tension $\gamma = 0$ and determined the equilibrium configurations of a unit cell with hexagonal symmetry. Taking the distance between the three-way junctions, L (Fig. 1*A*), as a parameter setting a constraint on the possible configurations, we minimized the bending energy for different values of the parameter L and found the corresponding energies, $F_E(L)$ (Fig. 1*B*). The equilibrium unit cell configurations are those for which $F_E(L)$ has local minima (Fig. 1*B*). For $R = \frac{24}{J_0}$, we found four equilibrium configurations (Fig. 1*A*) with practically equal energies (Fig. 1 *B*, *Inset*) such that they can be treated as energetically degenerated states of the system.

The size differences between the equilibrium configurations of the hexagonal unit cell are calibrated by a specific length, λ_P. Indeed, as demonstrated by Fig. 1*A*, the shapes of tubules connecting the junctions in the equilibrium configurations can be seen as composed of standard units, each consisting of a region of a widening followed by a narrowing. We will refer to such a unit as the peristaltic block characterized by the peristaltic length λ_P. The second, third, and fourth configurations in Fig. 1*A* have one, two, and three peristaltic blocks between the junctions, respectively. The most compact unit cell configuration in Fig. 1*A*, which has the size of $\lambda_0 \sim 3\frac{1}{J_0}$, does not accommodate any peristaltic block. The origin of the peristaltic length, λ_P, is related to a fundamental geometrical feature of periodic axially symmetric surfaces of constant total curvature called unduloids (21) whose peristaltic block length can vary in a narrow range between $\frac{4}{J_s}$ and $\frac{2\pi}{J_s}$ (*SI Appendix, Unduloids as axially symmetric shapes of constant mean curvature*).

Based on the super-resolution images, in addition to the hexagonal unit cells, the ER matrices contain unit cells of other symmetries (4). To account for this, we computed the equilibrium configurations of the pentagonal, quadratic, and triangular unit cells (Fig. 1*C*). The computations demonstrated that, independently of the symmetry, all network unit cells are constructed according to the same principle as described for the hexagonal case.

Generalizing, a polygonal unit cell upon a vanishing tension can adopt a discrete series of the equilibrium configurations characterized by the interjunction length

$$L_n = \lambda_0 + n\,\lambda_P, \quad [5]$$

where n is the number of the peristaltic blocks between the junctions, and λ_0 is the size of the most compact configuration (Fig. 1*D*).

The results obtained for vanishing tension $\gamma = 0$ enable a prediction of the effects of ultra-low tensions. Tensions substantially smaller than the characteristic value of $\kappa \cdot J_0^2$ practically do not change the membrane shapes determined by the intrinsic curvature J_0. At the same time, they substantially contribute to the system energy because of the area difference between the equilibrium configurations (Fig. 1*B*, red curve). The results for the equilibrium configuration energies accounting for the tension contribution (Eq. **4**) for $\gamma = \frac{1}{100}\kappa J_0^2 \cong 1$ μN/m are presented in Fig. 1 *B*, *Inset*, which shows that the shape of the smallest unit cell becomes the most energetically favorable. Hence, the model predicts that ultra-low tensions existing in ER tubules (18, 19) can remove the effective energy degeneration of the equilibrium network configurations in favor of the most compact one.

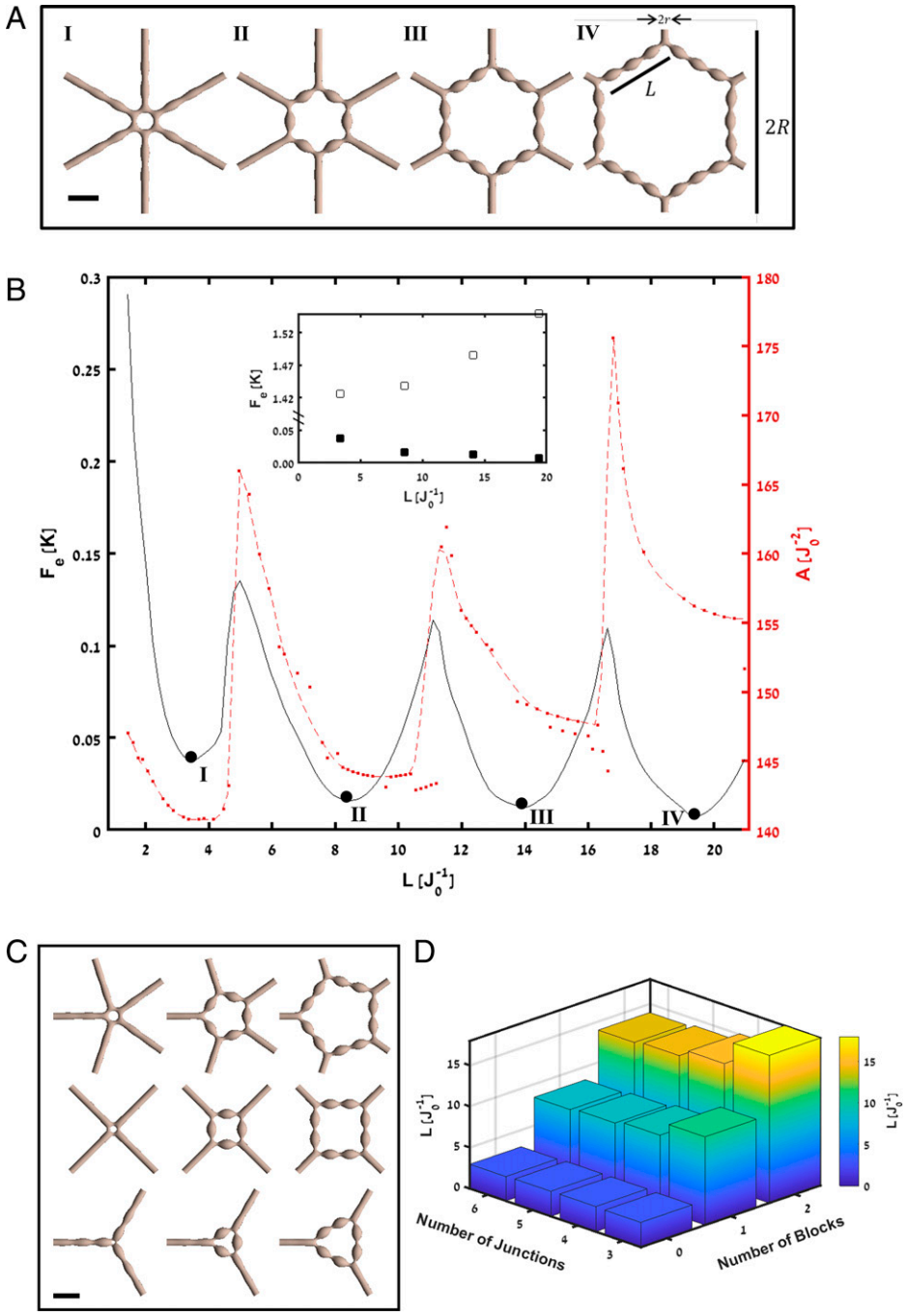

Fig. 1. Equilibrium configurations of a single unit cell of a polygonal network of membrane tubules. (*A*) The minimal energy configurations of a hexagonal unit cell corresponding to the minima of the energy profile presented in *B*. The numbers (I to IV) set the correspondence between the energy minima in *B* and conformations in *A*. (Scale bar, $8 \cdot J_0^{-1}$.) (*B*) The left axis and black curve represent the bending elastic energy of a hexagonal unit cell as a function of the distance between the neighboring junctions, *L*. The local minima correspond to the equilibrium configurations presented in *A*. The right axis and red curve represent the surface area of the configurations in dependence on *L*. The dots show the computed area values, whereas the dashed curve is an interpolation. (*Inset*) The effect of ultra-low membrane tension, $\gamma = \frac{1}{100}\kappa J_0^2$, on the energy of the equilibrium conformations. The solid and open squares represent the energies of the equilibrium conformations for $\gamma = 0$ and $\gamma = \frac{1}{100}\kappa J_0^2$, respectively. (*C*) Equilibrium configurations of the pentagonal, quadratic, and triangular unit cells. (Scale bar, $8 \cdot J_0^{-1}$.) (*D*) The dimension of the equilibrium unit cell configurations as a function of the junction number and the number of the peristaltic blocks between the junctions.

Network fragment of several unit cells. Using the same approach, we computed the equilibrium configurations of a tubular network fragment consisting of several hexagonal unit cells. The examples of the resulting configurations are presented in Fig. 2 *B* and *C*. While the membrane shapes and energies of the unit cells in this case slightly differ from those obtained for a single unit cell, these variations can be neglected compared to the accuracy of the experimental observations of the ER matrices. The major architectural principle described for single unit cells is valid also for the unit cells within networks: the equilibrium states can be presented as discrete conformational modes differing by the number of the peristaltic blocks between the three-way junctions.

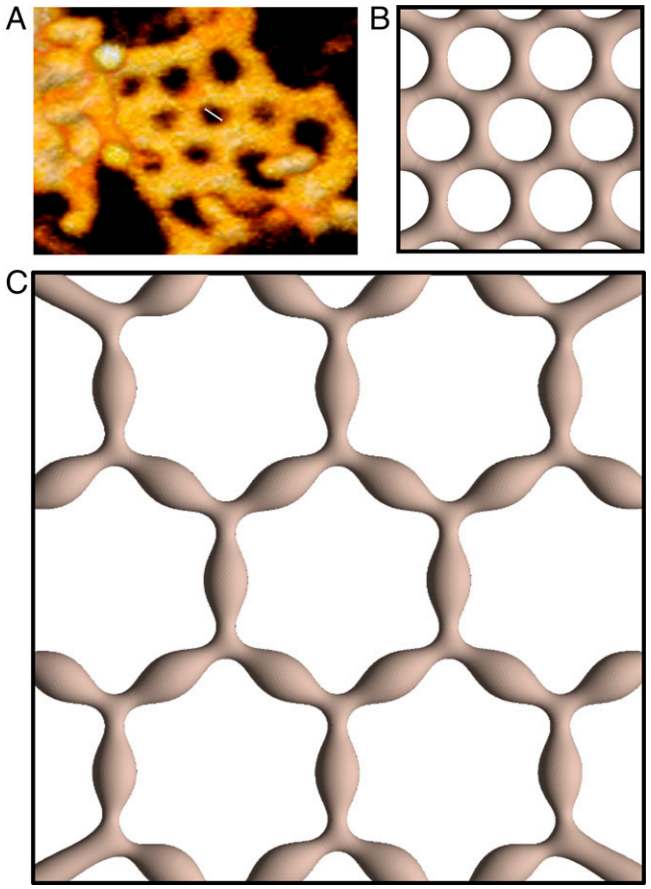

Fig. 2. Equilibrium configurations of a fragment of hexagonal tubular network. (*A*) Image of ER matrix showing a regular hexagonal lattice with typical unit cell size of ~ 50 *nm* as shown by the white bar within one of the unit cells. (Scale bar, 100 *nm*.) Adopted from ref. 4. (*B* and *C*) The computed configurations of an element or hexagonal tubular network for zero (*B*) and one (*C*) peristaltic blocks between neighboring junctions. Scale bars are represented by the box sides and are equal. (Scale bars, *B*, $16 \cdot J_0^{-1}$; *C*, $40 \cdot J_0^{-1}$.)

The computed conformation of the most compact equilibrium configuration of the hexagonal network fragment (Fig. 2*B*) closely resembles the one observed for ER tubular matrices (4) (Fig. 2*A*). A quantitative agreement between the experimental and computed configurations was reached for the intrinsic curvature value $J_0 = 0.025\ \mathrm{nm}^{-1}$, which is in a good agreement with the curvature of the surrounding ER tubules.

The conformations of other computed configurations could not be compared with the observed configurations because of strong fluctuations (4) of the network planes of the latter. Hence, the calculated interjunction distances of the extended conformations of the network unit cells represent the model predictions for future experiments.

Nanoholes in ER Sheets. The ER sheet nanoholes are located within flat regions of ER sheets (Fig. 3*A*), but their formation is essentially dependent on the curvature generating proteins of the reticulon family (5), which are otherwise responsible for formation of ER tubules and sheet edges. This implies that the nanohole rims originate directly from the tubules as a result of, for example, the shrinking of the tubular loops adjacent to the sheet edges (5). Therefore, we analyze a scenario in which nanoholes form as a result of collapse of the tubular network unit cells connected to the ER sheet edge (5). As stated in the previous sections, the effects of reticulons are accounted for by the intrinsic curvature J_0 of the tubules and the nanohole rims.

We consider the interface region between an ER tubular network and a sheet, which includes one network unit cell adjacent to the sheet edge and the associated boundary region of the sheet. We address two states of the system. In one state, the unit cell has a shape of a two-tined tubular fork whose ends are merged with the sheet edge (Fig. 3 *B*, *1* and *3*). In the alternative state, the fork is converted into one tubule connected directly to the sheet edge, whereas the space between the fork tines is transformed into a nanopore within the sheet (Fig. 3 *B*, *2* and *4*). The experimental image (Fig. 3 *A*, *Right*) obtained in ref. 5 exhibits these two system states.

The computed configurations of the two states are presented in Fig. 3 *B*, *1* and *2* for vanishing tension $\gamma = 0$ and in Fig. 3 *B*, *3* and *4* for an ultra-low tension, $\gamma = 2.5 \frac{\mu N}{m}$. The nanopore, whose typical computed shape is shown in Fig. 3*C*, is predicted to vary

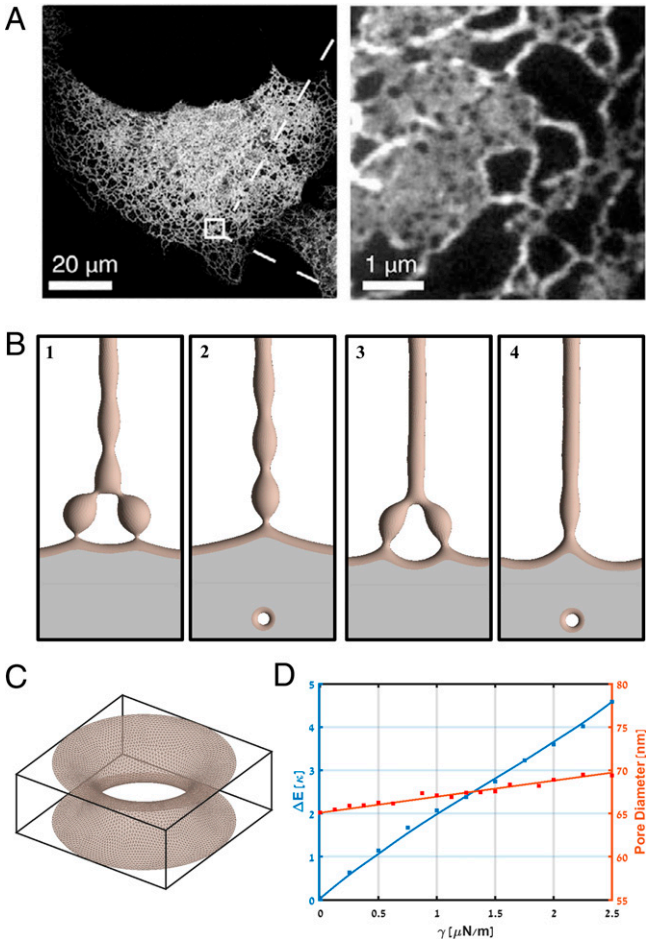

Fig. 3. Generation and structure of ER sheet nanoholes. (*A*) ER sheet nanohole image from Schroeder et al. (5) showing confocal (*Left*) and zoomed-in stimulated emission depletion microscopy (STED) (*Right*) images of ER sheets and tubules in mammalian cells with ~ 100 *nm* diameter nanoholes within the sheets. (*B*, 1–4) Computed equilibrium configurations of the interface region between a tubular network and a sheet: *1* and *2* for vanishing tension $\gamma = 0$, *3* and *4* for the ultra-low tension $\gamma = 2.5 \frac{\mu N}{m}$. The sheet thickness and the tubule intrinsic curvature are taken equal, respectively, to 50 *nm* and $J_0 = \frac{1}{50}\ nm^{-1}$ according to data from Schroeder et al. (5), and the membrane-bending rigidity is $\kappa = 20 \cdot k_B T$. Scale bars are represented by the box sides. (Scale bars, $16 \cdot J_0^{-1}$.) (*C*) Computed shape of a nanohole for vanishing tension $\gamma = 0$ with the luminal diameter ~ 65 *nm* (for $J_0 = \frac{1}{50}\ nm^{-1}$). (*D*) Left axis and blue graph represent the difference in the elastic energy between the equilibrium configurations without and with nanohole as a function of tension, γ. Right axis and red graph represent the luminal diameter of the nanohole as a function of the tension. The parameter values are $\kappa = 20 \cdot k_B T$ and $J_0 = \frac{1}{50}\ nm^{-1}$, and the sheet thickness is 50 *nm*.

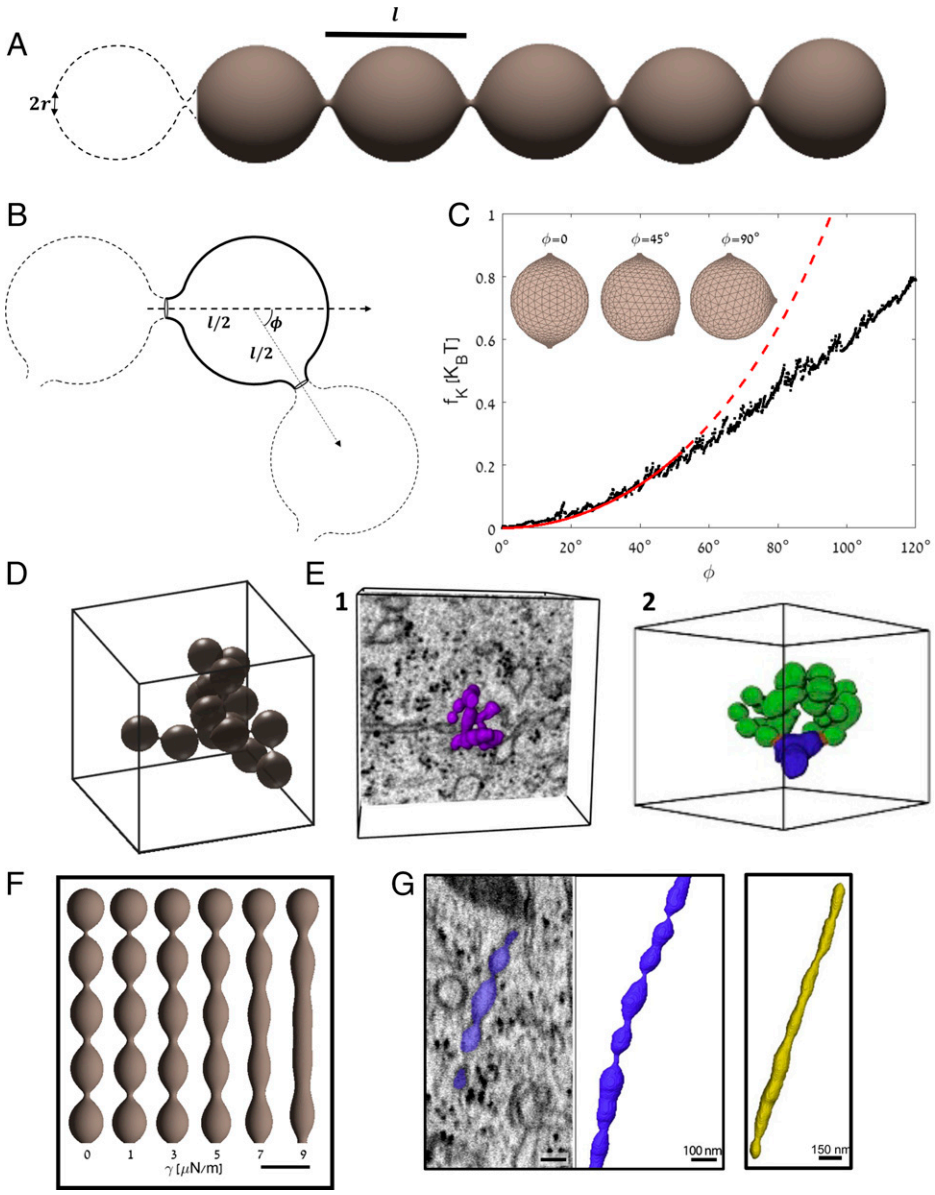

Fig. 4. ERES internal membrane organization and ER transport intermediate. (*A*) Bead chain–like equilibrium shape of a continuous membrane whose area, *A*, strongly exceeds the internal length scale set by the intrinsic curvature $A > J_0^{-2}$; the edge is constricted to a circle of a small radius, $r = 0.5\, J_0^{-1}$, and the tension vanishes, $\gamma = 0$. In the computations, the radii of the membrane necks were assumed to exceed the membrane thickness, which corresponds to $r \geq 0.1\, J_0^{-1}$. The dashed shape represents the possible continuity of the chain to any arbitrary number of beads. (*B*) Schematic representation (solid line) of one chain element consisting of a bead with the necks connecting it to the adjacent beads (dashed lines). The angle ϕ characterizes a kink of the chain axis mediating the chain bending. (*C*) The chain-bending energy per one chain element as a function of the kink angle ϕ. The black dots are the calculated energies. The red curve is a fit of Eq. **6** to the computational results in the angle range between 0 and 53°, which corresponds to the assumption of small curvatures, $J < l^{-1}$. (*Insets*) Computed shapes of the chain elements with different kink angles. (*D*) An example of a high-probability random orientation of a bead chain–like membrane configuration consisting of 15 elements and corresponding to a self-avoiding random walk. (Scale bars, $20 \cdot J_0^{-1}$.) Quantitative agreement with the observed configurations (*E*, *Left* and *Right*) is reached for $J_0 = 0.05 nm^{-1}$. (*E*) Observed configuration of ERES internal structure from Weigel et al. (6). (*Left*) The box dimension is $\sim 1.2\ \mu m$. (*Right*) The mean dimension of a chain element is $\sim 60\ nm$, and the mean size of the entire ERES is $\sim 360\ nm$. (*F*) Bead chain–like configurations under different membrane tensions. The chain length equals $26 \cdot J_0^{-1}$. (Scale bar, $5 \cdot J_0^{-1}$ (100 *nm* for $J_0 = \frac{1}{20}\ nm^{-1}$.) (*G*) Focused ion beam scanning electron microscopy (FIB-SEM) and three-dimensional rendering of transport intermediate from Weigel et al. (6).

its diameter as a function of the system parameters. For $J_0 = 0.02\, nm^{-1}$ and the sheet thickness of 50 nm, which correspond to the measurements by Schroeder et al. (5), the computed pore diameter is close to the experimentally observed value of about 100 nm (5) as presented in Fig. 3*D*. The shape of the nanopore rim under vanishing tension can be also expressed in a cumbersome but analytical form (22).

The computed difference of the energies of the two states (Fig. 3*D*) demonstrates that, for vanishing tension $\gamma = 0$, the state with and without the nanopore have equal energies, whereas an application of ultralow tension strongly favors the nanopore state (Fig. 3*D*).

ERES Internal Structure and Transport Intermediates. The super-resolution images of the grape-like ERES infrastructures (Fig. 4*E*) (6) reveal a large curvature of their constituent membranes but leave a question open about the topological properties of this membrane organization, which may be interpreted as an interwoven

tubular network of contiguous lipid bilayers (6) or, possibly, a spawn-like pile of densely interlinked but separate vesicles. Here, we propose a simple model for ERES internal architecture, which recovers its peculiar appearance and, in addition, provides a straightforward explanation of ERES transformation into the pearl chain–like transport intermediates (Fig. 4*G*) (6).

ERES internal structure. We propose ERES to be formed by a single continuous membrane patch with intrinsic curvature J_0 and a sufficiently large area A such that $A \gg \frac{1}{J_0^2}$. The edge of the patch is constricted into a little circle with radius $r < \frac{1}{J_0}$ (Fig. 4*A*) corresponding to the cross-section of a membrane nano-neck, which connects, according to the observations, the ERES membrane to the surrounding ER (6). Under normal conditions, we assume no tension to be imposed on the membrane $\gamma = 0$.

The shape of the membrane patch with minimal bending energy F_B is presented in Fig. 4*A* and has a character of a chain of nearly spherical membrane beads connected by thin membrane necks. In order to avoid the violation of the applicability of the continuous elastic model of membrane elasticity, in the numerical computations, we put a limit on the cross-sectional radii of the necks between the beads, r_n, which prevented them from adopting values smaller than the membrane thickness. The obtained detailed shapes in the narrow vicinity of the neck waists must be seen as having a semiquantitative character.

This type of configuration could be expected based on the tendency of the membrane to acquire a shape with total curvature, J, as close as possible to the constant intrinsic curvature J_0 at every point of the membrane surface as required by the minimization of the bending energy (Eqs. **2** and **3**). A well-known family of periodic tubular surfaces of constant total curvature, $J = const$, called unduloids includes the bead chain–like configurations (*SI Appendix*, *Unduloids as axially symmetric shapes of constant mean curvature*). The obtained membrane configuration (Fig. 4*A*) is close to the bead chain–like unduloid but slightly deviates from it because of two conflicting requirements imposed on the shape: the sealing of the chain end and the abovementioned constraint of the minimal possible radius of the interbead neck cross-section r_n (*SI Appendix*, Fig. S2*A*). The total curvature J of the computed shape (Fig. 4*A*) only marginally deviates from the constant values of J_0. Based on these results, a bead chain–like unduloid is a very good approximation for the computed shape.

The membrane bead chain (Fig. 4*A*) must be extremely flexible with respect to bending. Such bending occurs through the generation of kinks of the chain axis, which results from the sliding of the necks connecting the beads along the bead surfaces (Fig. 4*B*). To evaluate the chain flexibility, we assessed its effective flexural rigidity k_f. To this end, we performed an approximative computation of the shape and energy changes of a bead resulting from a relative shift of its two necks characterized by a kink angle ϕ(Fig. 4*B*). The computed kink energy change per bead $f_K(\phi)$, presented in Fig. 4*C*, can be expressed as a function of an effective bead chain curvature J_C, defined as the curvature of a circular arc of length, l_B, connecting the ends of the bead's necks (*SI Appendix*, Fig. S2*B*). The graphical definitions of and relationships between J_C, l_B, and the effective bead diameter l are presented in *SI Appendix*, *Approximative computation of kink energy of a membrane bead chain* and Fig. S2*B*. Assuming the bead chain curvature to be small, $J_C l < 1$, the kink energy can be presented in a quadratic approximation as

$$f_K = \frac{1}{2} k_f J_C^2 l_B, \qquad \textbf{[6]}$$

where the values of J_C and l_B are related to the kink angle ϕ and the bead diameter l by

$$J_C = \frac{2}{l}\tan\left(\frac{\phi}{2}\right), \text{ and } l_B = \frac{\phi}{J_C}. \qquad \textbf{[7]}$$

We fitted the computed energy $f_K(\phi)$ (Fig. 4*C*) to the function Eq. **6**, accounting for Eq. **7** and using the flexural rigidity k_f as a single fitting parameter, which resulted in

$$\kappa_f \cong 0.5 \cdot l \cdot k_B T. \qquad \textbf{[8]}$$

The conformation of a flexible bead chain has a statistical character since the chain is subject to strong thermal fluctuations and, similarly to a flexible polymer, is expected to adopt, on average, a folded conformation [see, for example (23)]. The average size of an effective globule formed by the folded chain can be best characterized by the rms distance between the chain ends, R_N. To estimate R_N, we consider the bead chain as an effective polymer consisting of elementary segments of length l_0. The l_0 value is determined by the largest between two intrinsic scale lengths of the bead chain. The first scale length is structural and equal to the bead diameter l. The second scale length is set by the chain flexural rigidity and represented by Kuhn length l_K of the effective polymer, which can be related to the polymer persistence length l_P by $l_K = 2l_P$ (23). Using the relationship between l_P and the chain flexural rigidity $l_p = \frac{\kappa_f}{k_B T}$ (23) and accounting for Eq. **8**, we obtain $l_p \approx \frac{1}{2} l$ and, hence, the Kuhn length $l_K \approx l$. Since the two intrinsic scale lengths have similar values, we consider the bead chain as a self-avoiding polymer with an elementary segment length equal to the bead diameter $l_0 = l$ and the segment number N equal to that of the beads. In this approximation, the end-to-end distance of the bead chain can be estimated according to (23):

$$R_N \approx l \cdot N^{\nu}, \qquad \textbf{[9]}$$

where $\nu \approx 0.6$ (23).

A typical high-probability conformation of the bead chain we obtained by computational simulations is presented in (Fig. 4*D*). Qualitatively, it agrees with the observed grape-like configurations of ERES infrastructure, two of which are given in Fig. 4*E* (6).

For a quantitative description of the system, we chose the value of the membrane intrinsic curvature $J_0 = 0.05nm^{-1}$ such that the computed bead cross-sectional diameter l corresponds to that of the observed average bulges composing the grape-like surface of ERES with $l \cong 60nm$ (6) (*SI Appendix*, *Approximative computation of kink energy of a membrane bead chain*). Taking, based on the images (6), a typical number of beads in the chain $N = 15$, the effective ERES size estimated according to Eq. **9** is $R_N \approx 300nm$, which is in a good agreement with the measurements (6).

Importantly, due to their flexibility, the ERES membrane bead chains are expected to exhibit persistent strong fluctuations around the average conformation.

ER transport intermediate. We propose that the pearl chain–like transport intermediates (6) (Fig. 4*G*) form directly from the initial bead chain–like ERES structures upon application to them of ultra-low pulling forces generated by the molecular motors running along the cytoskeletal microtubules (6).

The application of a pulling force has two effects on the bead chain. First, it straightens the initial folded chain conformation. Second, it generates membrane tension, γ, which may result in some degree of the bead stretching with respect to their tension-free shape.

We computed the bead chain conformations for membrane tension varying in the range $\gamma = (0-9)\frac{\mu N}{m^2}$, for the membrane intrinsic curvature $J_0 = 0.05nm^{-1}$ (Fig. 4*F*). The lowest tension configurations in Fig. 4*F* account for the chain straightening without any noticeable deformation of the membrane beads. This happens already for almost vanishing tensions produced by pulling forces, which can be estimated as $\frac{k_B T}{l}$ and, for the bead size of $l = 60nm$, are of the order of $10^{-2} pN$. For tensions close to $10\frac{\mu N}{m}$, the beads undergo some stretching, but the chain

retains its varicosities (Fig. 4*F*). Such tensions are generated by about 1-pN large pulling forces typical for the upper limit of a force produced by one molecular motor (24, 25). The bead chain–like shapes obtained for the tensions in the range (3 7) $\frac{\mu N}{m^2}$ (Fig. 4*F*) are the closest to the observed shapes of ER transport intermediates (Fig. 4*G*).

Discussion

Here, we proposed and computationally substantiated the physical mechanism of formation and stabilization of the membrane structures recently found at the nanoscopic level of organization of the peripheral ER: the ER tubular matrices (4) (Fig. 2*A*), the ER sheet nanoholes (5) (Fig. 3*A*), the ERES infrastructures (6) (Fig. 4*E*), and the pearl chain–like ER transport intermediates (6) (Fig. 4*G*).

Our analysis revealed a common structural motif underlying the geometry of most of the observed ER nanostructures. In the case of ER matrices, it is represented by the peristaltic blocks, which compose, as mosaic elements, the various matrix conformations characterized by different distances between the intertubular junctions. The basically same structural motif represents the bead elements of ERES structures and the repeating sections of the shapes of ER transport intermediates. The shape of this structural motif originates from the geometry of surfaces of constant nonzero mean curvature and more specifically from the periodic elements of unduloids.

According to our results, the geometry of all these ER nanostructures, which are characterized by the 50- 100-nm intrinsic length scales, is determined by a single factor, the intrinsic curvature of ER membranes. The intrinsic curvature can be generated by the dedicated proteins and/or protein complexes such as reticulon/REEP family proteins (2, 5, 9, 14), COPII or COPI coats (6, 26), or combinations between them.

The membrane tension, a second mechanical factor involved generally in intracellular membrane shaping, must either vanish in these nanostructures or have ultra-low values up to 10 μN/m. Ultra-low tensions have been suggested to exist in ER (18, 19). They can be generated by the elements of cytoskeleton interacting with ER membranes (6) or result from such generic factors as membrane thermal undulations or local fluctuations of the intratubular pressure (19).

We proposed ultra-low tension to play the role of modulator of the membrane configurations. The ER matrices are predicted to have, upon a vanishing tension, a discrete series of energetically degenerated conformations as shown by the low and nearly equal energies of the local equilibrium states represented by the energy minima (Fig. 1*A*). The application of an ultra-low tension is shown to favor the smallest unit cell configuration. We predicted ultra-low tensions to affect the structure of the interface region between the ER tubular network and ER sheet favoring formation of nanoholes within the sheet plane (Fig. 3*B*). For ERES, ultra-low tensions are proposed to drive the transformation of an entropically folded bead chain–like structure of the ERES internal membrane (Fig. 4*D*) to a stretched pearl chain–like shape (Fig. 4*F*) modeling the ER transport intermediates.

Materials and Methods

Numerical computations of the membrane conformation of the ER matrices, ER tubules and tubular loops adjacent to and merged with the sheet edges, the ER sheet nanoholes, the ERES bead conformations, and the ERES transport intermediates were performed by using a combination of MATLAB and the finite element method–based freeware the Surface Evolver. The MATLAB program controlled all parameters of each calculation. The elastic energy minimization was performed by the finite element approach using Kenneth Brakke's Surface Evolver. The computation efficiency was increased by accounting for the shape symmetry. The obtained minimal energy shape data were imported into MATLAB for further analysis and graphical output. For computations of the randomly folded conformations of the ERES bead chain, a MATLAB program randomly generated for each chain bead a kink angle and a rotation angle around the bond axis, picked the computed bead shape, and joined it to the bead chain. These steps were repeated N times according to the required total number of the beads. The fitting of Eq. **7** to the kink energy data of Fig. 4*C* was made using a MATLAB app. Also, the analytical shapes and their associated features were calculated using MATLAB.

Data Availability. All study data are included in the article and/or *SI Appendix*.

ACKNOWLEDGMENTS. We are grateful to Tom Rapoport and Jennifer Lippincott-Schwartz for stimulating discussions. M.M.K. was supported by Deutsche Forschungsgemeinschaft through Sonderforschungsbereich 958 "Scaffolding of Membranes" and Israel Science Foundation Grant 3292/19 and also holds the Joseph Klafter Chair in Biophysics.

1. D. S. Schwarz, M. D. Blower, The endoplasmic reticulum: Structure, function and response to cellular signaling. *Cell. Mol. Life Sci.* **73**, 79–94 (2016).
2. L. M. M. Westrate, J. E. E. Lee, W. A. A. Prinz, G. K. K. Voeltz, Form follows function: The importance of endoplasmic reticulum shape. *Annu. Rev. Biochem.* **84**, 791–811 (2015).
3. Y. Shibata, G. K. Voeltz, T. A. Rapoport, Rough sheets and smooth tubules. *Cell* **126**, 435–439 (2006).
4. J. Nixon-Abell *et al.*, Increased spatiotemporal resolution reveals highly dynamic dense tubular matrices in the peripheral ER. *Science* **354**, aaf3928 (2016).
5. L. K. Schroeder *et al.*, Dynamic nanoscale morphology of the ER surveyed by STED microscopy. *J. Cell Biol.* **218**, 83–96 (2019).
6. A. V. Weigel, *et al.*, ER-to-Golgi protein delivery through an interwoven, tubular network extending from ER. *Cell* **184**, 2412–2429.e16 (2021).
7. M. Puhka, M. Joensuu, H. Vihinen, I. Belevich, E. Jokitalo, Progressive sheet-to-tubule transformation is a general mechanism for endoplasmic reticulum partitioning in dividing mammalian cells. *Mol. Biol. Cell* **23**, 2424–2432 (2012).
8. M. West, N. Zurek, A. Hoenger, G. K. Voeltz, A 3D analysis of yeast ER structure reveals how ER domains are organized by membrane curvature. *J. Cell Biol.* **193**, 333–346 (2011).
9. F. Di Sano, P. Bernardoni, M. Piacentini, The reticulons: Guardians of the structure and function of the endoplasmic reticulum. *Exp. Cell Res.* **318**, 1201–1207 (2012).
10. N. Wang *et al.*, Mechanism of membrane-curvature generation by ER-tubule shaping proteins. *Nat. Commun.* **12**, 11–15 (2021).
11. G. Orso *et al.*, Homotypic fusion of ER membranes requires the dynamin-like GTPase atlastin. *Nature* **460**, 978–983 (2009).
12. M. M. Kozlov, "Spontaneous and intrinsic curvature of lipid membranes: Back to the origins" in *Physics of Biological Membranes*, P. Bassereau, P. Sens, Eds. (Springer, Cham, 2018), pp. 287–309.
13. W. Helfrich, Elastic properties of lipid bilayers: Theory and possible experiments. *Z. Naturforsch. C* **28**, 693–703 (1973).
14. J. Hu *et al.*, Membrane proteins of the endoplasmic reticulum induce high-curvature tubules. *Science* **319**, 1247–1250 (2008).
15. G. K. Voeltz, M. M. Rolls, T. A. Rapoport, Structural organization of the endoplasmic reticulum. *EMBO Rep.* **3**, 944–950 (2002).
16. M. Terasaki, Axonal endoplasmic reticulum is very narrow. *J. Cell Sci.* **131**, jcs210450 (2018).
17. R. Dimova, Recent developments in the field of bending rigidity measurements on membranes. *Adv. Colloid Interface Sci.* **208**, 225–234 (2014).
18. C. Lin, Y. Zhang, I. Sparkes, P. Ashwin, Structure and dynamics of ER: Minimal networks and biophysical constraints. *Biophys. J.* **107**, 763–772 (2014).
19. P. Georgiades *et al.*, The flexibility and dynamics of the tubules in the endoplasmic reticulum. *Sci. Rep.* **7**, 16474 (2017).
20. K. A. Brakke, The surface evolver. *Exp. Math.* **1**, 141–165 (1992).
21. M. Hadzhilazova, I. M. Mladenov, J. Oprea, Unduloids and their geometry. *Arch. Math.* **43**, 417–429 (2007).
22. M. Hadzhilazova, J. F. Ganghoffer, I. M. Mladenov, Membrane fusion based on the geometry of the stalk model. *Mech. Res. Commun.* **63**, 54–60 (2015).
23. M. Rubinstein, R. H. Colby, *Polymer Physics* (Oxford University Press, 2003).
24. J. T. Finer, R. M. Simmons, J. A. Spudich, Single myosin molecule mechanics: Piconewton forces and nanometre steps. *Nature* **368**, 113–119 (1994).
25. J. T. Finer, A. D. Mehta, J. A. Spudich, Characterization of single actin-myosin interactions. *Biophys. J.* **68**, 291S–296S (1995).
26. M. Okamoto *et al.*, High-curvature domains of the ER are important for the organization of ER exit sites in *Saccharomyces cerevisiae*. *J. Cell Sci.* **125**, 3412–3420 (2012).